Climate Dynamics (2021) 57:1445–1461
https://doi.org/10.1007/s00382-020-05594-8

ENSO teleconnections in an ensemble of CORDEX-CORE regional simulations

José Abraham Torres-Alavez[1] · Filippo Giorgi[1] · Fred Kucharski[1] · Erika Coppola[1] · Lorena Castro-García[2]

Received: 31 March 2020 / Accepted: 15 December 2020 / Published online: 2 January 2021

Abstract
Recent high-spatial-resolution regional simulations from the global program, coordinated regional climate downscaling experiment-coordinated output for regional evaluations (CORDEX-CORE), are examined to evaluate the capability of regional climate models (RCMs) to represent the El Niño–Southern Oscillation (ENSO) precipitation and surface air temperature teleconnections over five regions of the world. We find that the ensemble and individual RCM simulations generally preserve the broad regional scale ENSO signal from the general circulation models (GCMs) over different regions around of the world, reproducing the majority of the observed regional responses to ENSO forcing. Furthermore, in some cases, the RCM ensemble and individual models can improve the spatial pattern of teleconnections and the amplitudes of these patterns compared to the driving global models. Among such cases are the precipitation teleconnections over southern Africa, North America and the Arabian–Asian region. Our study presents the first analysis of ENSO teleconnections in GCM-driven RCMs over multiple regions, and it clearly shows the potential value of using such models non only in a climate change research context, but also in seasonal to annual prediction.

Keywords ENSO · Teleconnections · Regional climate models · Boreal winter · Precipitation · Surface air temperature

1 Introduction

The El Niño–Southern Oscillation (ENSO) is the world's leading mode of interannual climate variability (Trenberth et al. 1998; Langenbrunner and Neelin 2013; Ward et al. 2014; Chiodi and Harrison 2015). It affects the climate of many regions of the world, such as the tropics (Wang et al. 2004; McPhaden et al. 2006; Kucharski et al. 2007), the Pacific–North American region (Wallace and Gutzler 1981; Herceg Bulić 2010), South America (Kayano et al. 2009), the Arabian Peninsula (Abid et al. 2018) and southern Africa (Dieppois et al. 2015). Both ENSO warm (El Niño) and cold (La Niña) events can produce floods and droughts over different regions, particularly in the tropics, with large socio-economic impacts (Ropelewski and Halpert 1987; Philander 1990; Diaz et al. 2001; King et al. 2016). Consequently, recent studies have increasingly focused on investigating the ENSO's connection to climate, towards a better understandings of climate prediction and the effects of climate change on ENSO.

In recent decades, the main tools for understanding ENSO dynamics and associated teleconnections have been general circulation models of the coupled atmosphere–ocean system (GCMs; Latif et al. 2001; Guilyardi et al. 2004, 2009; Achuta Rao and Sperber 2006; Herceg Bulić and Kucharski 2012; Bellenger et al. 2013; Weare 2013). Several studies showed some ability of GCMs to reproduce ENSO precipitation teleconnections (Joseph and Nigam 2006; Cai et al. 2010). These studies suggest that the problems demonstrated in reproducing ENSO teleconnection patterns can be related to the difficulty of the GCMs to represent adequately the spatial pattern and amplitude of the main sea surface temperature (SST) anomalies in the equatorial Pacific (Joseph and Nigam 2006; Coelho and Goddard 2009).

Other authors have examined simulations of the coupled model intercomparison project (CMIP) forced by observed SSTs (Spencer and Slingo, 2003; Cash et al. 2005; Langenbrunner and Neelin 2013). These studies have found

✉ José Abraham Torres-Alavez
jtorres@ictp.it

[1] Earth System Physics, The Abdus Salam International Centre for Theoretical Physics (ICTP), Trieste, Italy

[2] Department of Chemical and Biochemical Engineering and Center for Global and Regional Environmental Research, The University of Iowa, Iowa City, IA, USA

substantial differences between simulations and observations in different teleconnection regions. For example, Langenbrunner and Neelin (2013) found spatial correlation coefficients less than 0.5 between CMIP5 models and observations, but with a good agreement in the amplitude of the precipitation response. This demonstrates the challenge that models face to accurately simulate regional signals.

On the other hand, regional climate models (RCMs) are increasingly being used to produce high resolution climate change information for impact assessment applications and climate service activities (e.g. Giorgi 2019). It is thus important that RCMs are able to simulate the regional to local teleconnection response of leading modes of climate variability such as ENSO. This response is determined by two factors: the large scale information entering the RCM domain from the lateral boundaries and a possible modulation of this ENSO large scale signal by regional and local forcings, such as topography, coastlines and landuse. A good simulation of ENSO teleconnections by an RCM thus requires, on the one hand, a good simulation of the ENSO large scale responses by the driving model (e.g. GCM or reanalysis), and a good performance by the RCM in preserving this large scale signal and possibly enhance it through the model's higher resolution.

Despite the importance of ENSO teleconnections for local impacts and the increasing use of RCM information for impact studies, the literature on analyses of ENSO teleconnections in RCMs is relatively scarce. Several studies have analysed ENSO signals in RCMs driven by reanalysis data as initial and lateral boundary conditions. They have found that the RCMs can simulate the main features of the ENSO precipitation teleconnection response in different regions of the world when realistic large scale variability drives the models (e.g. Tourigny and Jones 2009; Mariotti et al. 2011; McGlone and Vuille 2012; Boulard et al. 2012; Endris et al. 2013; Llopart et al. 2014; Zaroug et al. 2014; Whan and Zwiers 2016; Ratna et al. 2017; King and Vincent 2018). Fewer studies have addressed the issue of ENSO teleconnections in RCMs driven by GCMs either for present day conditions or within a climate change context. For example, Meque and Abiodun (2015) analyzed the ENSO-precipitation teleconnection signal over Southern Africa in an ensemble of 10 RCM simulations driven by analyses of observations and different GCMs and found widely varying performance across the models, strongly depending on the driving fields. Similar conclusions were found by Jiang et al. (2013), who investigated the performance of 10 GCM-driven RCM simulations over North America. Endris et al. (2018) assessed the ENSO signal over Eastern Africa and its changes for the late twenty-first century in an ensemble of 2 RCM simulations driven by 4 GCMs, again finding widely varying response associated both to the differences in the driving GCMs and nested RCM physics. Da Rocha et al. (2014) have used three GCM downscaled by RegCM4 and they found that both GCMs and RegCM4 members are able to capture the ENSO driven anomalies in present day climate but RegCM4 improves the signal over southeastern South America (SA). Both ensembles project the same kind of precipitation anomalies change (increase over southeastern SA and decrease over northern–northeastern SA) with a weaker relation between ENSO and precipitation compared to the present day. Clearly, there is a need of further and more systematic investigations on how GCM-RCM systems can simulate regional ENSO teleconnection patterns around the globe.

A good opportunity for such a study is given by the recent completion of a coordinated set of RCM projections as part of the coordinated regional climate downscaling experiment (CORDEX-CORE) program (Gutowski et al. 2016; Giorgi and Gutowski 2015). It consists of simulations for the period 1970–2099 with two RCMs, the RegCM4 (Giorgi et al. 2012) and REMO (Jacob et al. 2012 and Remedio et al. 2019), run at 25-km grid spacing over nine CORDEX domains for two greenhouse gas concentration scenarios, where each RCM is driven by three GCMs, In this study, we thus examine the capability of these GCM-RCM systems to reproduce the impact of ENSO teleconnections over different domains, with the ultimate goals of (i) identifying whether the driving GCMs reproduce the observed large scale ENSO teleconnection patterns; (ii) assess whether the ENSO signal propagates correctly from the driving GCMs to the RCMs; (iii) assess whether the higher resolution of the RCMs locally modulates the ENSO signal. Specifically, we examine the spatial patterns and magnitude of the ENSO effects on precipitation and surface air temperature, and focus on five regions where ENSO effects are important.

Here we focus only on present day conditions, since this analysis is necessary before examining eventual changes in the characteristics of ENSO and its teleconnections in future climate projections, work which is under way and will be presented in future papers. Compared to previous studies, we use for the first time a consistent analysis of a coordinated multi GCM-RCM high resolution ensemble over multiple domains, and our study is especially important as a reference for the use of the CORDEX-CORE dataset in impact and vulnerability assessments.

We begin our analysis with a description of the data and methods in Sect. 2 followed by a discussion of the results in Sect. 3 and main conclusions in Sect. 4.

2 Datasets and analysis

In this study, ENSO precipitation teleconnection patterns are studied for RCM and GCM simulations over the period 1975–2004, focusing on the December–January–February

(DJF) season. We emphasize that this analysis period is taken from uninitialized GCM projections with no assimilation of observations, and therefore the simulations are not expected to capture individual specific events (e.g. the El Nino of 1998) but can be assessed only in a statistical sense. We compare the model simulations with observed monthly mean SST and precipitation data during DJF for the years 1981–2010. For SST observations, we use the Hadley Centre Sea Ice and SST analysis dataset, HadISST (Rayner et al. 2003), while monthly precipitation is from the multi-source weighted-ensemble precipitation (MSWEP) V2 dataset, which is based on a combination of rain-gauge measurements, satellite products and reanalysis data (Beck et al. 2017a, b). This dataset showed good performance in describing precipitation over tropical regions (Zhang et al. 2019; Torres-Alavez et al. 2020), and its horizontal resolution is 25 km, same as the grid size of the RCM simulations. For surface air temperature assessment, we use data from the ERA5 reanalysis (Hersbach and Dee 2016).

The CMIP5 and CORDEX-CORE simulations are detailed in Tables 1 and 2. The regional climate simulations, six per domain, were performed with the latest version of the ICTP Regional Climate Model (RegCM4; Giorgi et al. 2012) and REMO (Jacob et al. 2012; Remedio et al. 2019) following the specifications of the CORDEX-CORE protocol. The CORDEX-CORE initiative is aimed at providing a set of homogeneous, downscaled regional climate projections over nine domains covering the majority of land areas of the world for use in impact and adaptation studies (Gutowski et al. 2016). In particular, as mentioned, we focus on four

Table 1 GCMs and RegCM4 configurations used in this study

Domain/LLJ	Driving GCMs/resolution	Physics scheme	Namelist option	Reference
Africa		Boundary layer	Holtslag	Holtslag et al. (1990)
	HadGEM2-ES (Jones et al. 2011)/1.25°×1.85°	Cumulus (land)	Tiedtke	Tiedtke (1996)
	MPI-ESM-MR (Stevens et al. 2013)/1.8653°×1.875°	Cumulus (ocean)	Kain–Fritsch	Kain and Fritsch (1990), Kain (2004)
	NorESM1-M (Zhang et al. 2019)/1.8947°×2.5°	Microphysics	SUBEX	Pal et al. (2000)
		Ocean flux	Zeng et al.	Zeng et al. (1998)
Central America and North America		Boundary layer	Holtslag	
	HadGEM2-ES/1.25°×1.85°	Cumulus (land)	Emanuel	Emanuel (1991)
	MPI-ESM-MR/1.8653°×1.875°	Cumulus (ocean)	Kain–Fritsch	
	GFDL-ESM2M (Dunne et al. 2012)/2.0225°×2.5°	Microphysics	SUBEX	
		Ocean flux	Zeng et al.	
South America		Boundary layer	Holtslag	
	HadGEM2-ES/1.25°×1.85°	Cumulus (land)	Tiedtke	
	MPI-ESM-MR/1.8653°×1.875°	Cumulus (ocean)	Kain–Fritsch	
	NorESM1-M/1.8947°×2.5°	Microphysics	SUBEX	
		Ocean flux	Zeng et al.	
Asia		Boundary layer	UW PBL	Grenier and Bretherton (2001), Bretherton and Park (2009), Bretherton et al. (2004)
	MPI-ESM-MR/1.8653°×1.875°	Cumulus (land)	Emanuel	
	NorESM1-M/1.8947°×2.5°	Cumulus (ocean)	Tiedtke	
	MIROC5 (Watanabe et al. 2010)/1.4008°×1.40625°	Microphysics	SUBEX	
		Ocean flux	Zeng et al.	

Table 2 GCMs and REMO-GERICS configurations used in this study

Driving GCMs	Physics scheme	Parametrization	Reference
HadGEM2-ES (Jones et al. 2011)	Boundary layer	Monin–Obukhov similarity theory	Louis (1979)
NorESM1-M (Bentsen et al. 2013)	Cumulus	Tiedtke with modifications	Tiedtke (1989) Nordeng (1994) and Pfeiner (2006)
MPI-ESM-LR (1.8°×1.8°) (Giorgetta et al. 2013)	Microphysics	Lohmann and Roeckner	Lohmann and Roeckner (1996)

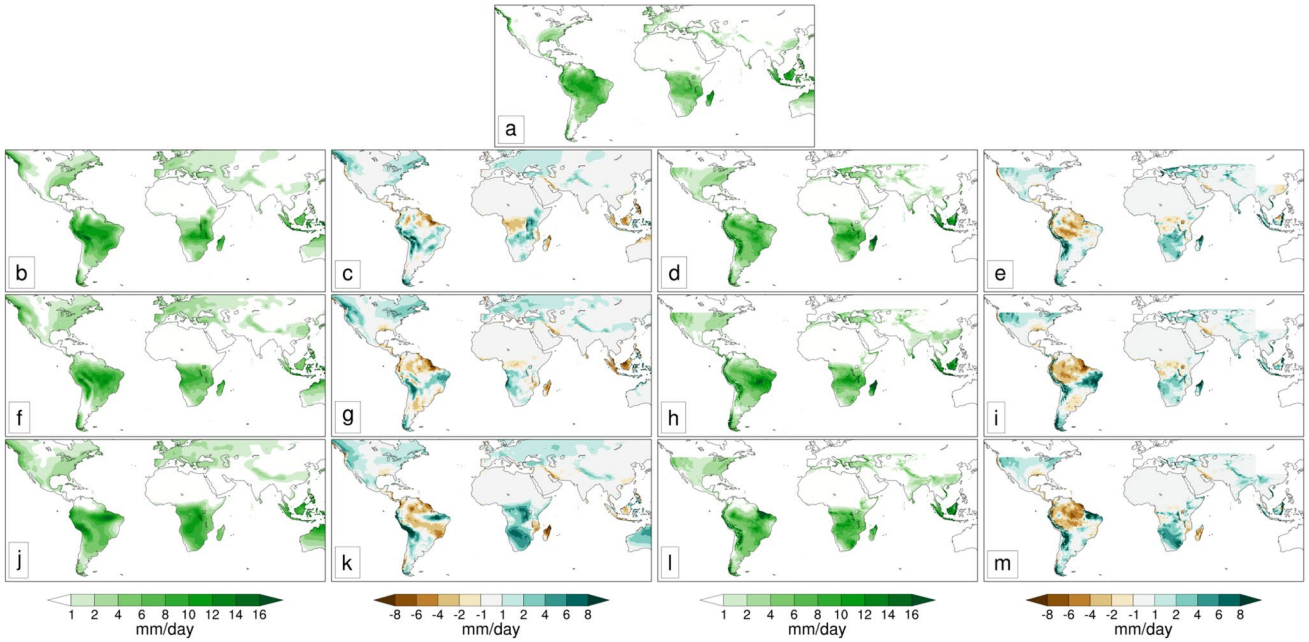

Fig. 1 DJF mean precipitation for: **a** MSWEP, **b** HadGEM2-ES and MIROC5 GCMs, **d** RegCM4 HadGEM2-ES and RegCM4 MIROC5, **f** MPI-ESM-MR GCM, **h** RegCM4 MPI-ESM-MR, **j** NorESM1-M and GFDL-ESM2M GCMs, and **l** RegCM4 NorESM1-M and RegCM4 GFDL-ESM2M; and precipitation differences for **c** HadGEM2-ES and MIROC5 GCMs minus MSWEP, **e** RegCM4 HadGEM2-ES and RegCM4 MIROC5 minus MSWEP, **g** MPI-ESM-MR GCM minus MSWEP, **i** RegCM4 MPI-ESM-MR minus MSWEP, **k** NorESM1-M and GFDL-ESM2M GCMs minus MSWEP, and **m** RegCM4 NorESM1-M and RegCM4 GFDL-ESM2M minus MSWEP. The units are mm/day

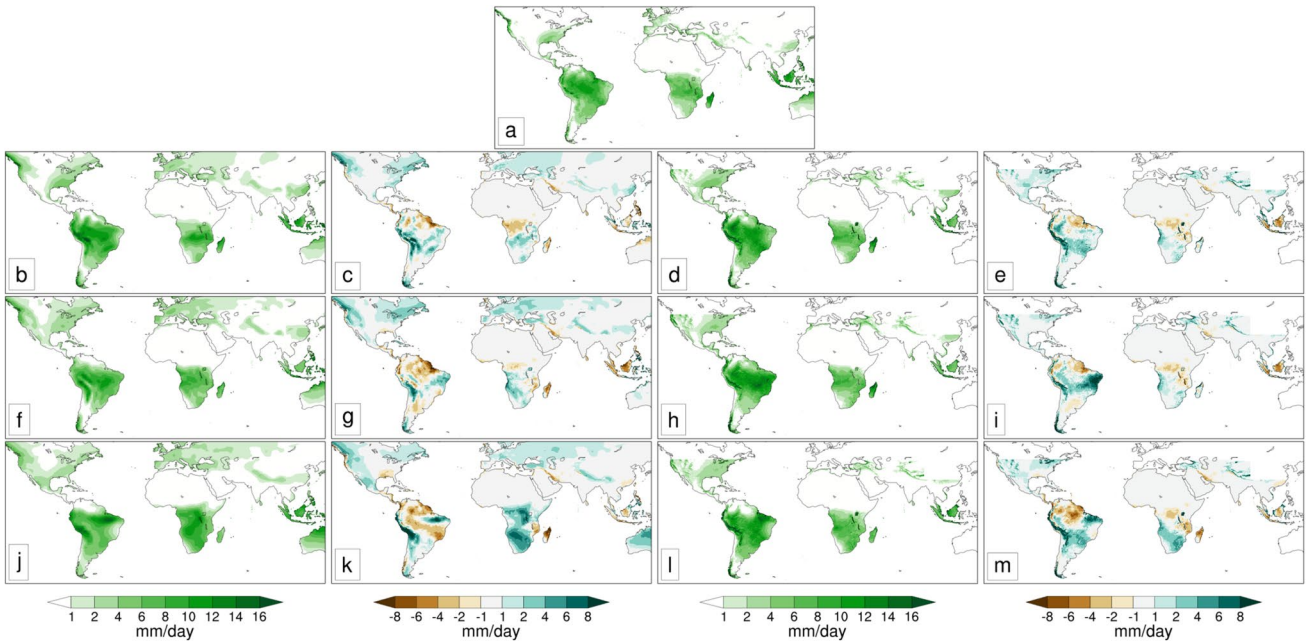

Fig. 2 DJF mean precipitation for: **a** MSWEP, **b** HadGEM2-ES GCM, **d** REMO HadGEM2-ES, **f** MPI-ESM-LR GCM, **h** REMO MPI-ESM-LR, **j** NorESM1-M GCM, and **l** REMO NorESM1-M; and precipitation differences for **c** HadGEM2-ES GCM minus MSWEP, **e** REMO HadGEM2-ES minus MSWEP, **g** MPI-ESM-LR GCM minus MSWEP, **i** REMO MPI-ESM-LR minus MSWEP, **k** NorESM1-M GCM minus MSWEP, and **m** REMO NorESM1-M minus MSWEP. The units are mm/day

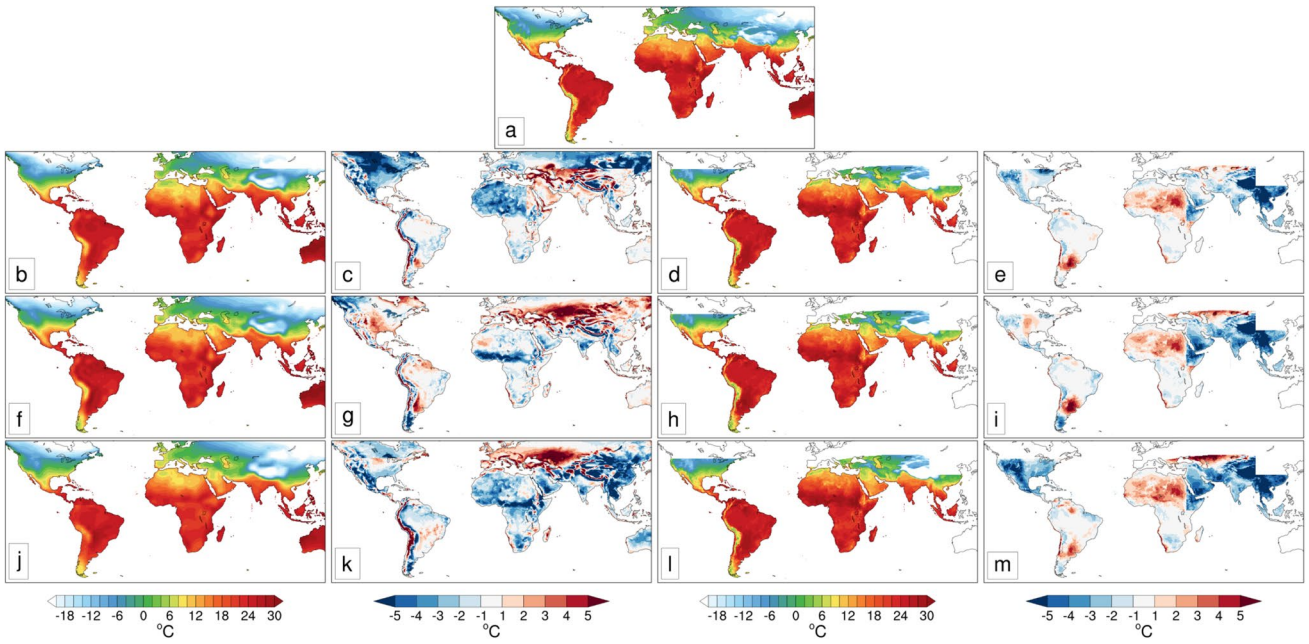

Fig. 3 As in Fig. 1, but for 2-m air surface temperature. The units are °C

domains where ENSO effects are stronger: Africa, Central/North America, South Asia and South America.

For each domain, the models are driven by three different GCMs from the CMIP5 ensemble (Taylor et al. 2012) and use a horizontal grid spacing of ~ 25 km. Each RCM has capability of using different physics parameterizations, and Table 1 reports the choice of scheme made for each domain based on preliminary test simulations aimed at optimizing the model performance. The GCMs were chosen based on two criteria: (1) they approximately cover the range of climate sensitivities in the CMIP5 ensemble (Taylor et al. 2012), since they have a low-(NorESM1-M), medium-(MPI-ESM-MR), and high-(HadGEM2-ES) equilibrium climate sensitivity; and (2) they show a generally good performance over the different

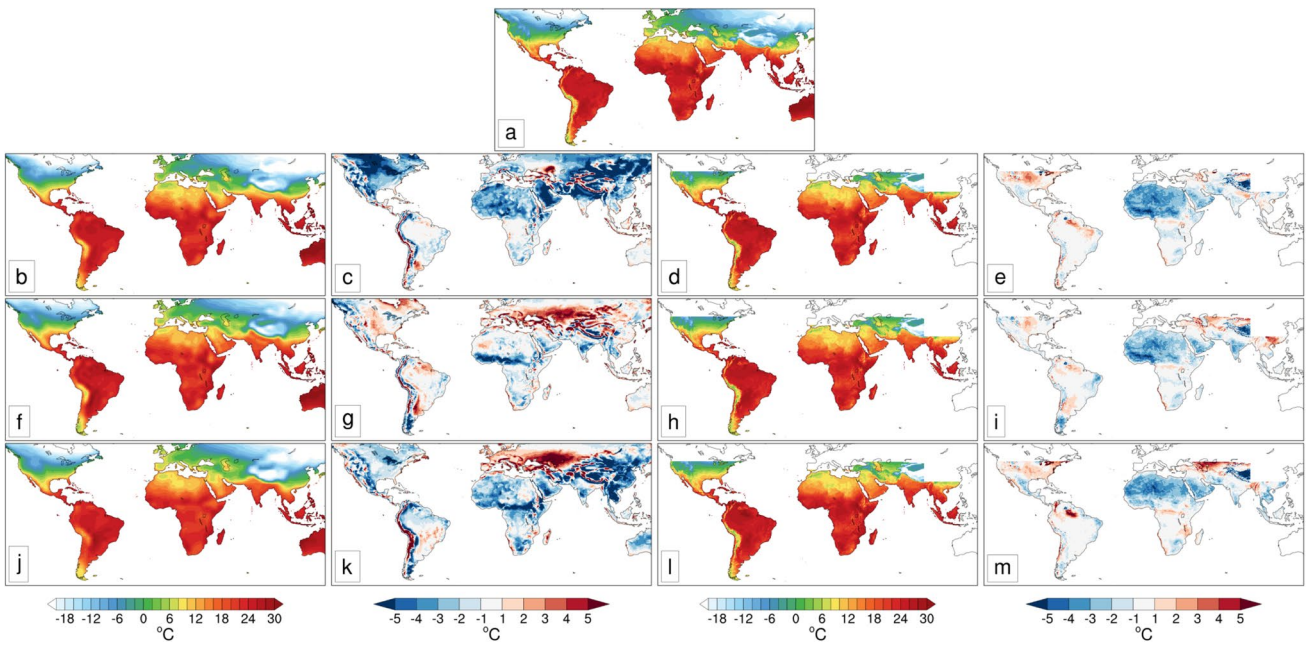

Fig. 4 As in Fig. 2, but for 2-m air surface temperature. The units are °C

CORDEX domains (e.g. Elguindi et al. 2014). However, for some domains, exceptions occur. Specifically, over the South Asia domain, HadGEM2-ES does not have a good simulation of the Indian monsoon (Ashfaq et al. 2017) and over the Central America domain NorESM1-M does not have a good representation of the dynamics of the region, in particular concerning the generation of tropical storms (McSweeney et al. 2015). For these reasons a choice was made within the RegCM4 community to use MIROC5 as driver over the South Asia domain and GFDL-ESM2M over the Central America/North America domain, models that in both cases exhibit a better performance based on some preliminary analysis.

All simulated precipitation data are regridded to the MSWEP grid prior to calculating the teleconnection patterns to facilitate the direct comparison of simulated and observed teleconnections. Linear regression is used to calculate the DJF precipitation (temperature) teleconnection patterns by projecting the normalized Niño-3.4 index (average SST from 5° S to 5° N and 190° to 240° E) onto the precipitation (temperature) field. A permutation test is applied to calculate the statistical significance of the regression coefficients (Manly 1997). The test first computes the regression coefficient for the original data. Then, a permutation resampling from the data without replacement is performed and the regression coefficient in the permuted data is re-computed. This is repeated n times, and for our study we generated 2000 permutations, as done in Taylor and MacKinnon (2012). The significance value is the proportion of permuted regression coefficients higher than the original regression coefficient.

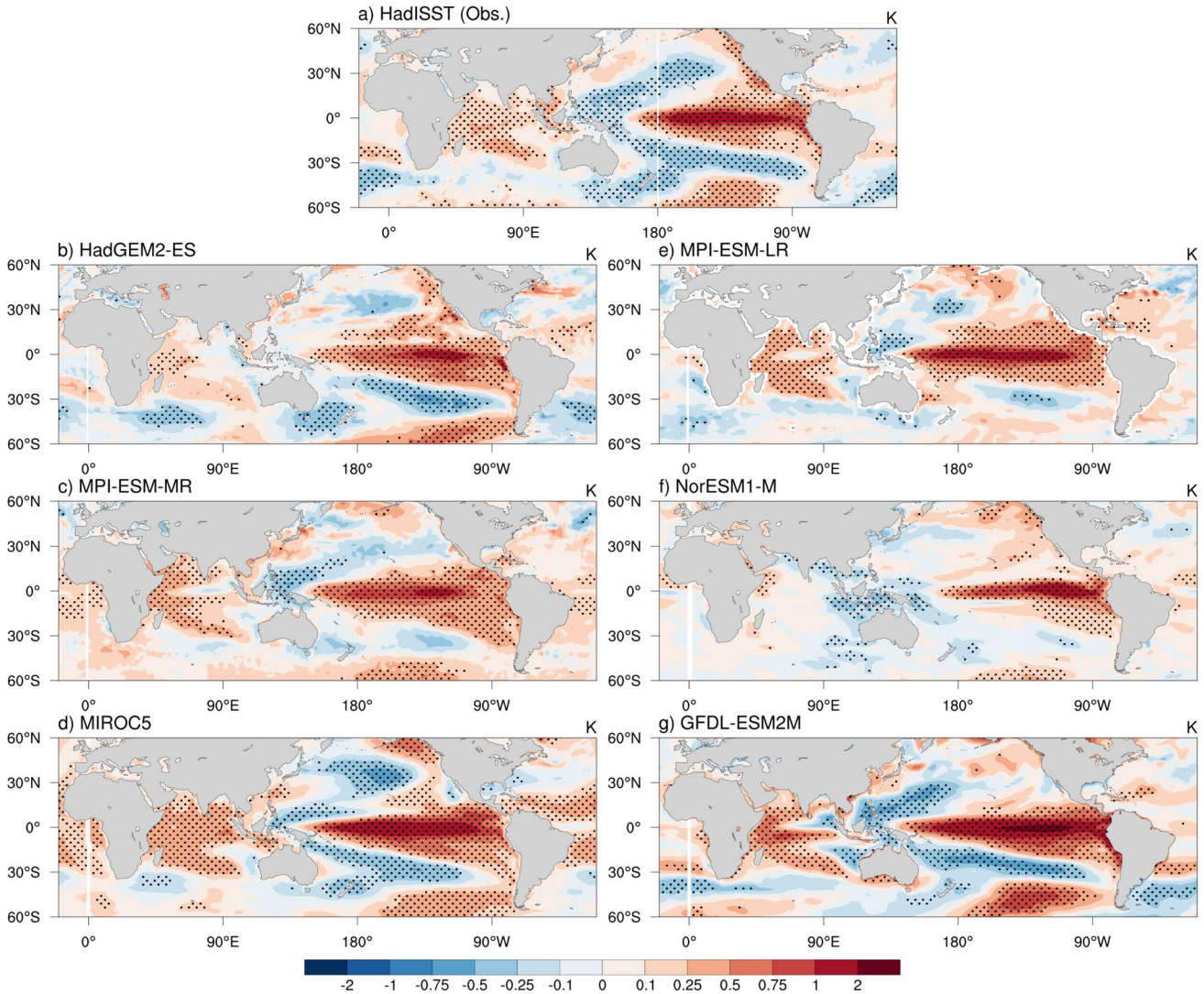

Fig. 5 Regression analysis of the El Niño 3.4 index to the boreal winter SST for **a** observations from HadISST during 1981–2010; **b** HadGEM2-ES; **c** MPI-ESM-MR; **d** MIROC5; **e** MPI-ESM-LR; **f** NorESM1-M; and **g** GFDL-ESM2M. The stippling indicates the point where the regression coefficient is statistically significant at a 95% confidence level. The units are K

Finally, we analyze the results of a multi-model ensemble following Langenbrunner and Neelin (2013), who perform the regression over all the models' simultaneously concatenated time series.

3 Results

3.1 Basic performance evaluation of the RCMs

In this section we present a first order evaluation of the DJF model precipitation and temperature climatologies as reference for the ENSO analysis to follow. The spatial distribution of the December–February (DJF) precipitation, as obtained from the MSWEP observations, the GCM and RegCM4 ensembles, and the corresponding bias, are presented in Fig. 1. In the observed field (MSWEP, Fig. 1a), the highest values of precipitation occur over Amazonia, southern Africa and the Maritime Continent. Both the GCMs and RegCM4 capture the main features of precipitation, as depicted by the observed dataset. However, the GCMs (Fig. 1c, g, k) show biases in some regions, particularly an underestimation over South America, Central America and the Maritime Continent, and an overestimation over southern Africa, with the largest bias for the NorESM1-M. In the RegCM4 simulations (Fig. 1e, i, m) the signs of the bias are similar to those in the GCMs in almost all the regions, with the exception of the Maritime Continent, where the RegCM4 shows a smaller bias. Over Mexico and southern Africa, the RegCM4 also show a smaller bias than the GCMs, particularly for the GFDL-ESM2M. However, over the northern part of South America, the dry bias is larger in the RegCM4 simulations.

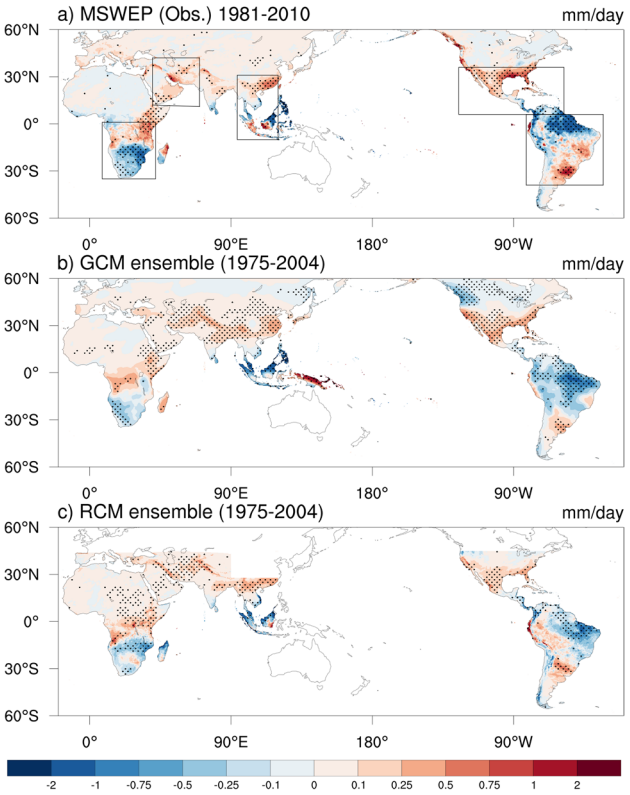

Fig. 6 Regression analysis of the El Niño 3.4 index to the boreal winter precipitation for **a** observations from MSWEP in the period 1981–2010; **b** GCM ensemble and **c** RCM ensemble. The stippling indicates the grid point where the regression coefficient is statistically significant at a 95% confidence level. The units are mm/day

Figure 2 shows the same information as in Fig. 1, but for the REMO simulations. REMO exhibits an overestimation of precipitation over Mexico, South America and southern Africa, and an underestimation in the Maritime Continent and in the equatorial part of South America and Africa. Comparing the biases between the RegCM4 and REMO simulations, the latter show a smaller bias over Africa and India, while the RegCM4 simulations show better performance over Mexico, the USA and the Maritime Continent. Over the northern part of South America, both RCMs show a dry bias, larger in the RegCM4 while REMO exhibits a wet bias over La Plata Basin.

Figure 3 shows the DJF surface air temperature for the ERA5 reanalysis, GCM and RegCM4, as well as the simulation biases relative to the ERA5. The ERA5 (Fig. 3a) exhibits the highest temperatures in the southern hemisphere and the equatorial region of Africa and South America and minimum temperatures in the USA, Canada and Himalayas. The HadGEM2-ES GCM (Fig. 3c) and NorESM1-M GCM (Fig. 3k) show a cold bias over North America, Africa and parts of Asia, particularly for the NorESM1-M. The RegCM4 simulations reduce the bias over North America, the Andes and southern Africa, while India and the Arabic Peninsula show a larger cold bias than the GCMs. Over the Sahara, the GCMs and RegCM4 show different biases, with a warm bias for the RegCM4. Figure 4 is similar to Fig. 3 but for the REMO model. The REMO simulations show a better representation of temperature than the GCMs in almost all regions, except the Sahara. For the surface air temperature, the biases are generally smaller in the REMO than the RegCM4 runs, particularly over the Arabic Peninsula, India and the La Plata Basin. Only over the southern part of Africa does the RegCM4 show lower biases.

Overall, as generally found in these types of analyses, the models reproduce the basic features of the observed climatologies, but with biases that vary from region to region both in sign and magnitude, and it is difficult to attribute model errors to specific causes. Other papers in this special issue, and most noticeably Teichmann et al. (2020) and Coppola et al (2020), present a more comprehensive analysis of different aspect of model performance,

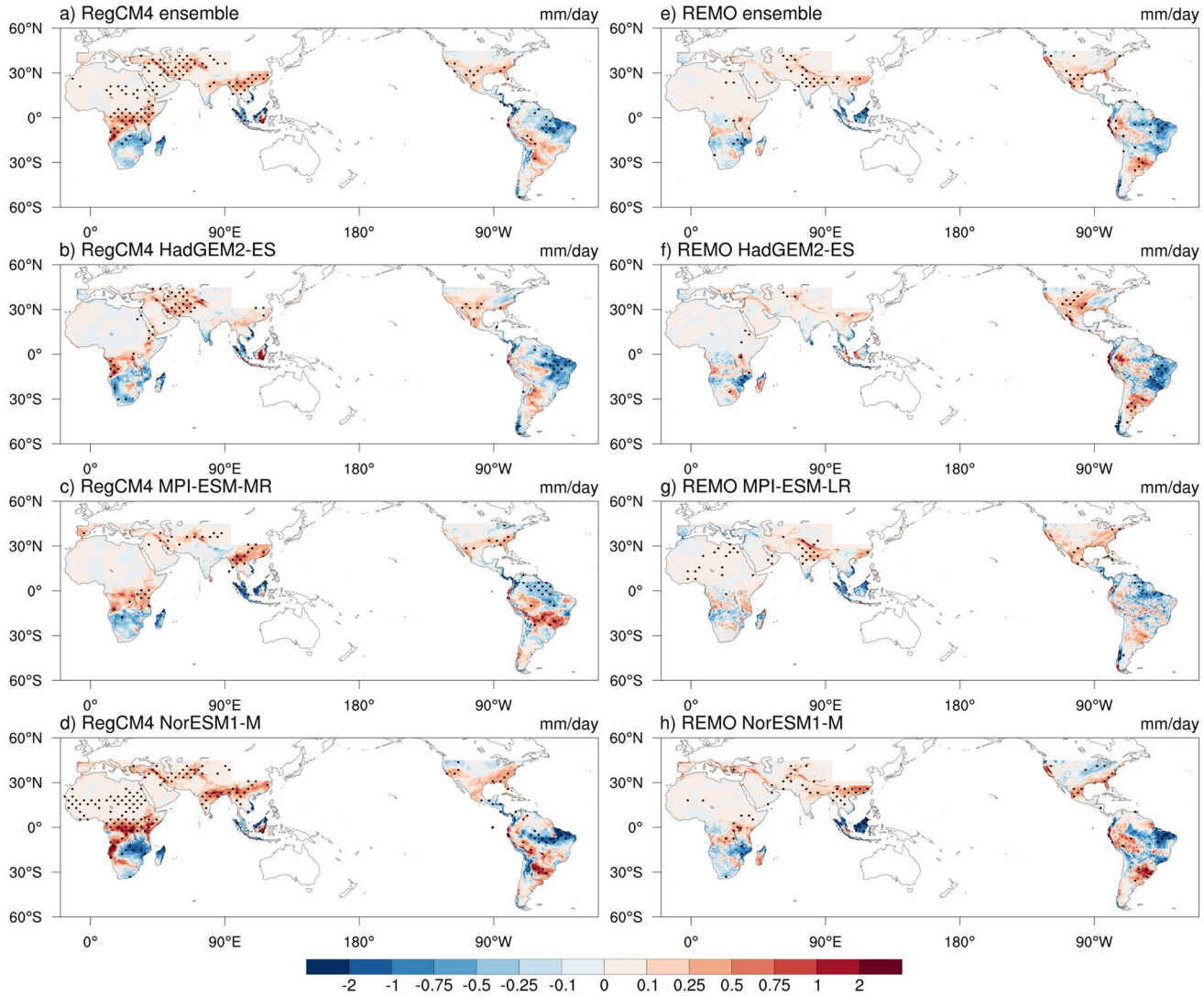

Fig. 7 Regression analysis of the Niño 3.4 index to the precipitation for **a** RegCM4 ensemble, the RegCM4 driven by **b** HadGEM2-ES; **c** MPI-ESM-MR; **d** NorESM1-M, **e** REMO-GERICS ensemble and REMO-GERICS driven by **f** HadGEM2-ES; **g** MPI-ESM-LR; and **h** NorESM1-M. The stippling indicates the grid point where the regression coefficient is statistically significant at a 95% confidence level. The units are mm/day

from means to extremes. Here we focus on the interannual variability as affected by the ENSO phenomenon, as detailed in the next sections.

3.2 Representation of ENSO SST anomalies in the GCMs

Before examining the teleconnection patterns in the RCMs, it is important to evaluate the ability of the CMIP5 models driving the RCM simulations in representing the El Niño 3.4 SST variability. DJF SST regressions with the El Niño 3.4 index for observations and CMIP5 models are shown in Fig. 5, where areas are highlighted in which the regression is significant at the 95% level. Note that the MIROC5 and GFDL-ESM2M are only used over two domains (Table 1) for the RegCM4 simulations. As expected, observed amplitudes are largest in the eastern equatorial Pacific (~2 K), with negative responses over the South and North Pacific and significant warming over the Indian Ocean. Overall, the simulated pattern and magnitude are comparable to those observed. However, almost all models show a westward extension of the positive SST

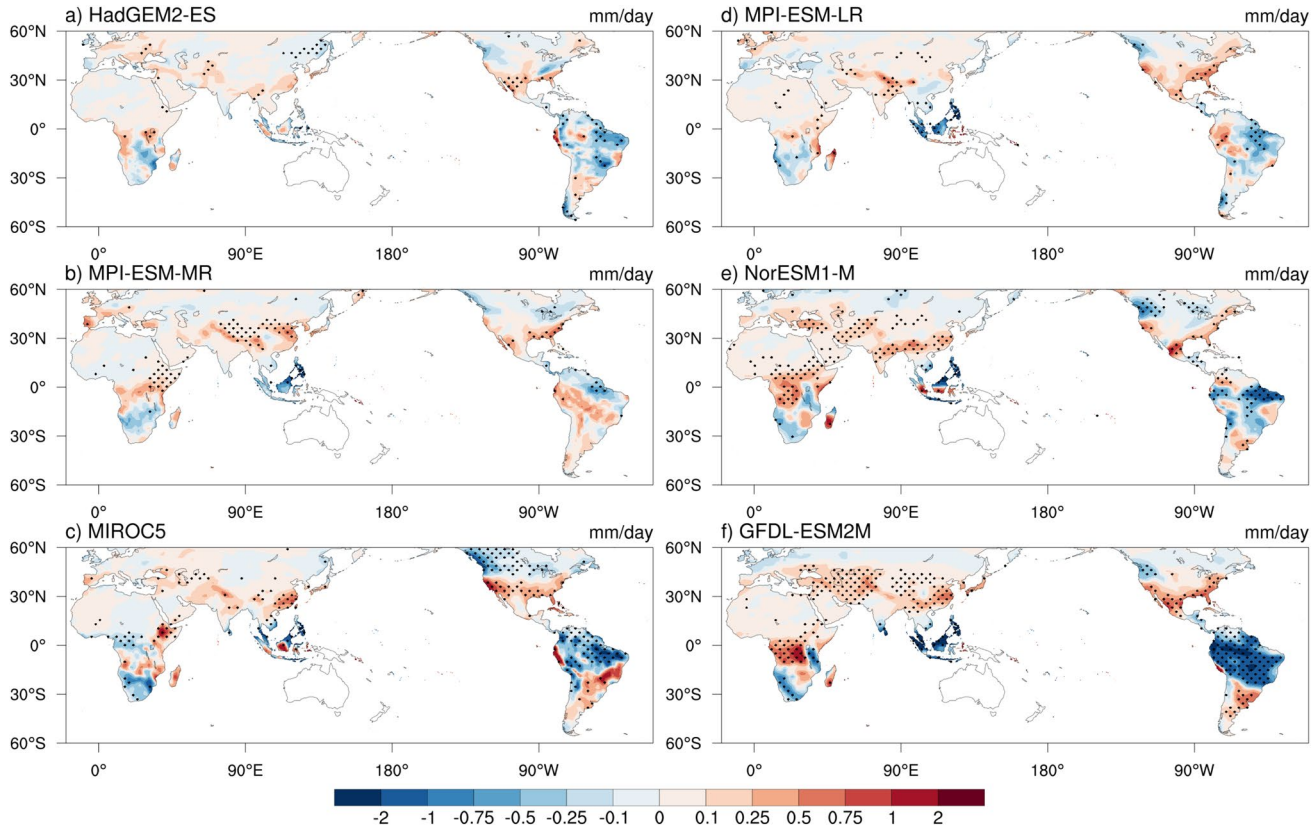

Fig. 8 Regression analysis of the Niño 3.4 index to the precipitation for **a** HadGEM2-ES GCM; **b** MPI-ESM-MR GCM; **c** MIROC5 GCM; **d** MPI-ESM-LR GCM; **e** NorESM1-M GCM and **f** GFDL-ESM2M GCM. The stippling indicates the grid point where the regression coefficient is statistically significant at a 95% confidence level. The units are mm/day

anomalies, with the exception of the NorESM1-M, which simulates a confinement of SST warming to the equatorial latitudes. In fact, this model shows a weak response everywhere else. The MIROC5 and GFDL-ESM2M regressions are excessively strong, particularly in the Pacific Ocean, while the MPI-ESM-MR ones are weak. With the exception of the North Pacific Ocean, the HadGEM2-ES exhibits reasonable distributions in most ocean basins.

3.3 Precipitation teleconnection patterns

Figure 6 shows the DJF precipitation regression pattern for the MSWEP data (Fig. 6a), the GCM (Fig. 6b) and RCM (Fig. 6c) ensembles onto the El Niño 3.4 index for a 30-year period. As can be seen in Fig. 6a, ENSO leads to a substantial reduction of precipitation over southern Africa, the northern part of South America and a large portion of the Maritime Continent, with an opposite pattern over the Arabian Peninsula, Eastern China, subtropical North America and La Plata Basin. The agreement between models (GCMs and RCMs) and observations is overall very good, as both ensembles (Fig. 6b, c) show the correct spatial patterns, but with a weak signal compared to the observations. The ensemble of RCMs improves the amplitude of the precipitation response of the GCMs over southern Africa, Central America and South America, North India and South of China, although deficiencies of both ensembles are found over North America and North Africa.

Towards a more detailed understanding of the teleconnection patterns in the RCM ensemble, Fig. 7 shows individual RCM simulation patterns (Fig. 7a–h). It shows that ENSO precipitation has a realistic amplitude in the RegCM4 (Fig. 7a–d) simulations, especially over Africa, Asia and South America, even producing regions of statistical significance. The REMO simulations (Fig. 7e–h), in contrast, produce a relatively weak ENSO signal in Africa, China and the Middle East, explaining the smoothed teleconnection patterns in the RCM ensemble mean.

To estimate potential improvements of dynamic downscaling in reproducing the ENSO signal, we compared the signal of the DJF precipitation regression pattern for the GCM (Fig. 8) and RCM (Fig. 7) simulations. For the HadGEM2-ES, both RCMs improve the amplitude and spatial pattern of the signal produced by the GCM in different regions. The RegCM4 driven by HadGEM2-ES produces a better response over southern Africa (although not

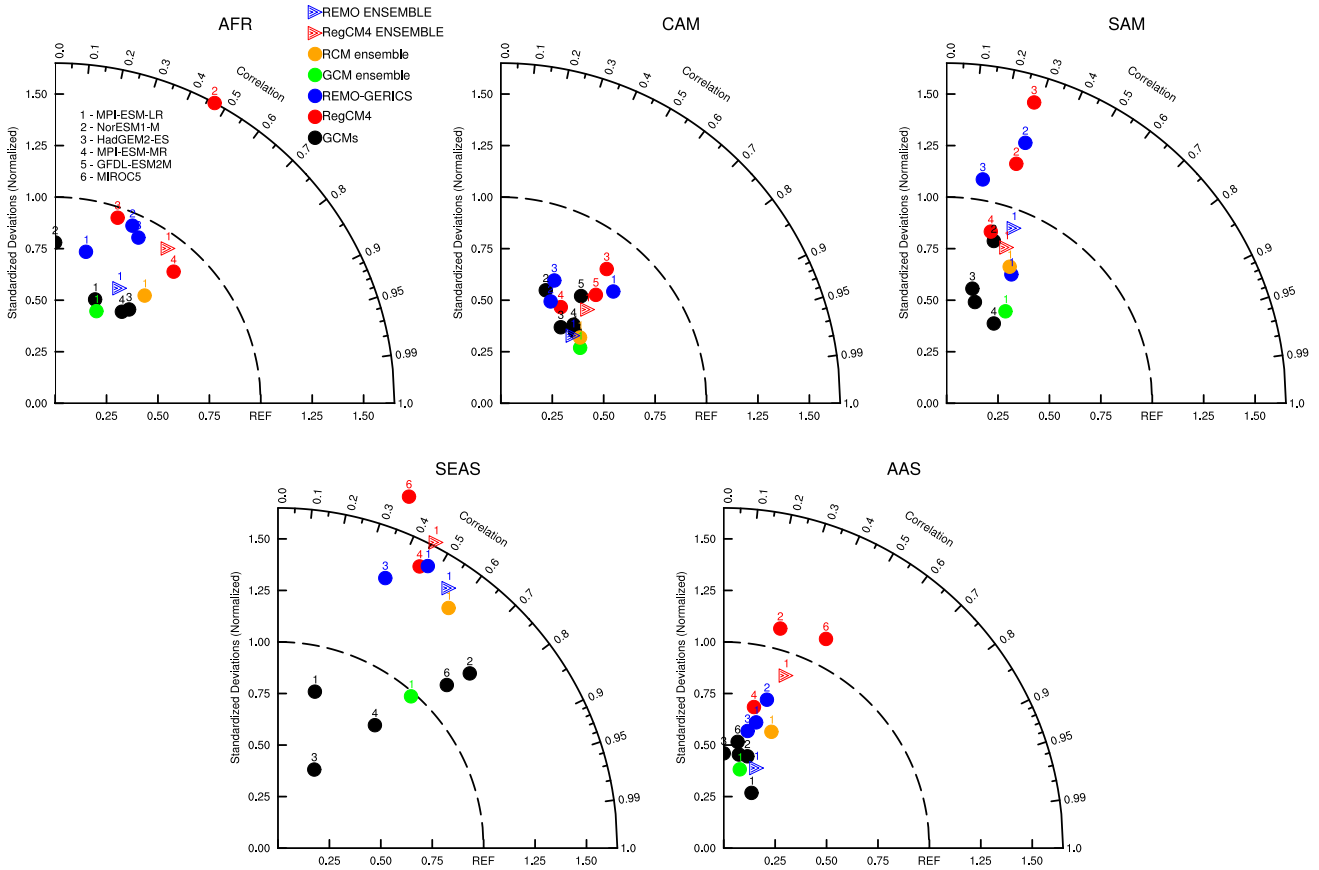

Fig. 9 Taylor diagrams for the standardized amplitude and spatial correlation of precipitation teleconnections in five regions, **a** southern Africa (AFR), **b** North and Central America (CAM), **c** South America (SAM), **d** Southeast Asia (SEAS) and **e** Arabian–Asian region (AAS). On the Taylor diagrams, angular axes show spatial correlations between modeled and observed teleconnections; radial axes show spatial standard deviation (root-mean-square deviation) of the teleconnection signals in each area, normalized against that of the observations. Black, red, blue, green and orange circles denote each of the GCM, RegCM4, REMO-GERICS, and GCM and RCM ensemble, respectively. Red and blue triangle denote RegCM4 and REMO-GERICS ensemble, respectively

significant at the 95% confidence level in all regions), and the Maritime Continent, while in the USA, Mexico and the La Plata basin, both RCMs show a better spatial pattern than the HadGEM2-ES, but the amplitude produced in REMO is closer to the observations. The RegCM4 simulations driven by MPI-ESM-MR show a more realistic and significant signal than the GCMs over southern Africa, South America and the Middle East. On the other hand, the REMO simulations driven by the MPI-ESM-LR do not show a significant improvement with respect to the GCM. The RCMs driven by NorESM1-M exhibit a signal amplitude that is substantially greater and closer to the observations than that of the GCM, particularly the RegCM4 over southern Africa and the Middle East. In particular, over the Middle East, the RegCM4 driven by MIROC5 show a stronger and more significant signal compared to the MIROC5 GCM, while over North America the GFDL-ESM2M GCM show a slightly stronger and realistic signal than the RegCM4 GFDL-ESM2M.

For a more detailed regional analysis, we focus on five regions of robust and significant ENSO response in observations enclosed in the boxes shown in Fig. 6a. They include (a) southern Africa (AFR); (b) North and Central America (CAM); (c) South America (SAM); (d) Southeast Asia (SEAS); (e) Arabian–Asian region (AAS). The first four regions are characterized by a north–south dipole pattern of ENSO precipitation response signal, while the AAS shows a positive DJF ENSO signal. Figure 9 presents the Taylor diagrams for each of these regions. These diagrams show the spatial correlations between observed and simulated ENSO precipitation response for each model plotted against the spatial standard deviation normalized by the observed one. The latter is used as a measure of the spatial variability of the teleconnection amplitude. Note that each RCM simulation is forced by a different GCM in a given region (Tables 1, 2), and individual simulations with small negative correlations with observations are not displayed in the diagrams.

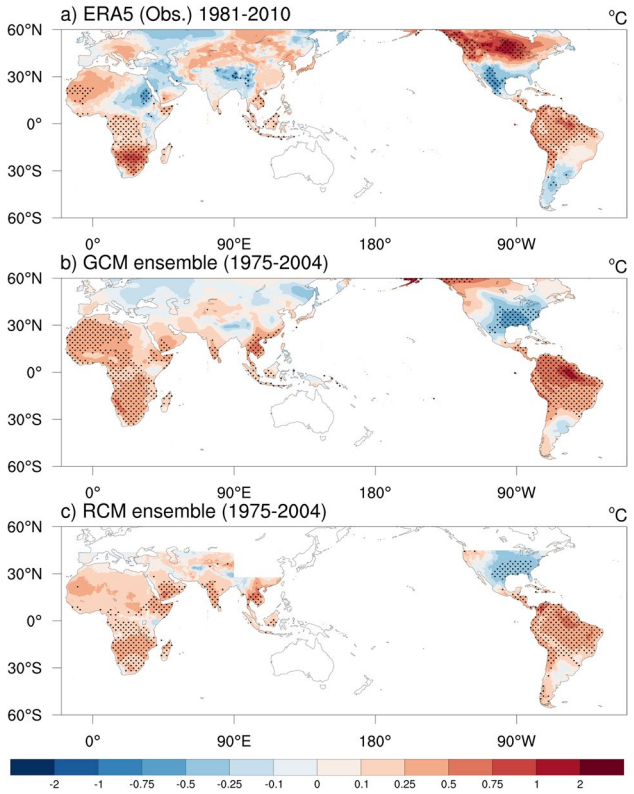

Fig. 10 As in Fig. 6, but for 2-m air surface temperature. The units are °C

Overall, the RCMs' spatial variation of the signal's amplitude is substantially greater than that of the GCMs, and it is closer to observations in every region, with the exception of the Southeast Asia region. Concerning correlations, the differences between GCMs and RCMs are more mixed across models and regions. In almost all regions, the RegCM4 and REMO ensembles are more accurate in reproducing spatial patterns than most of the GCMs; specifically, the RegCM4 ensemble shows the best performance for Africa and the Arabian–Asian region and the REMO ensemble over South America. Overall, the correlations with observations are not very high, less than 0.7.

3.4 Two-meter surface air temperature teleconnection patterns

The observed and simulated changes in 2-m temperature anomaly patterns associated with ENSO are shown in Fig. 10. The observed ENSO response is characterized by a warming over southern and western Africa, northern South America, Central America and southeastern Asia, with a significant cooling impact over Mexico and the southern United States, Northeast African and the Arabian Peninsula (Fig. 10a). The ENSO teleconnection is reasonably well simulated by both the GCMs and RCMs, except for the cooling pattern over Northeast Africa, the Arabian Peninsula, the region of the North America monsoon and southern South America. In addition, both ensembles show a slightly weaker signal than observed in the region of strong warming over southern Africa. The magnitude of the signal in the RCM ensemble matches better the observed pattern than do the GCMs over western Africa, northern South America and the United States. In addition, the GCMs show regions with teleconnection signals at the 95% confidence level non present in the observations over the North Sahara, southeastern United States and India, the latter two being present also in the RCM ensemble.

Essentially, all individual simulations clearly show signals and patterns that generally match the observed ones over almost all the regions (Fig. 11). An exception is the Arabian–Asian region, which is only reproduced by the RCM simulations driven by the HadGEM2-ES. In fact, the HadGEM2-ES has considerably better ENSO signals in all the domains compared to the other GCMs (Fig. 11b, e). Also, the RCMs are able to simulate some teleconnection signals significant at the 95% confidence level displayed in the observations (e.g. Africa and South America).

Comparing the DJF 2-m temperature anomaly patterns associated with ENSO in the RCMs (Fig. 11) and GCMs (Fig. 12), the HadGEM2-ES GCM shows a more realistic amplitude over Africa than the RCMs, which exhibit a weaker signal there than the GCMs, particularly REMO, which produces non-significant signals. Over North America and South America, the amplitude of the signal is conserved from the GCM to the RCMs for both the HadGEM2-ES and MPI-ESM driven runs. In these simulations, the spatial pattern and amplitude of the signal are similar for the GCMs and RCMs. For the NorESM1-M, the RCM simulations conserve the spatial pattern of the GCM but with a stronger signal and closer to the observations. The RegCM4 MIROC5 simulation also shows a stronger and realistic signal over the Middle East and Arabian Peninsula than the MIROC5 GCM, while over North America, the RegCM4 GFDL-ESM2M weakens the amplitude of the teleconnection pattern of the GCM.

Figure 13 shows the Taylor diagrams for the response of surface temperature to ENSO over the various hot-spot regions. In this case, RCM and GCM ensembles show comparable skills and the correlations are mostly lower than 0.8.

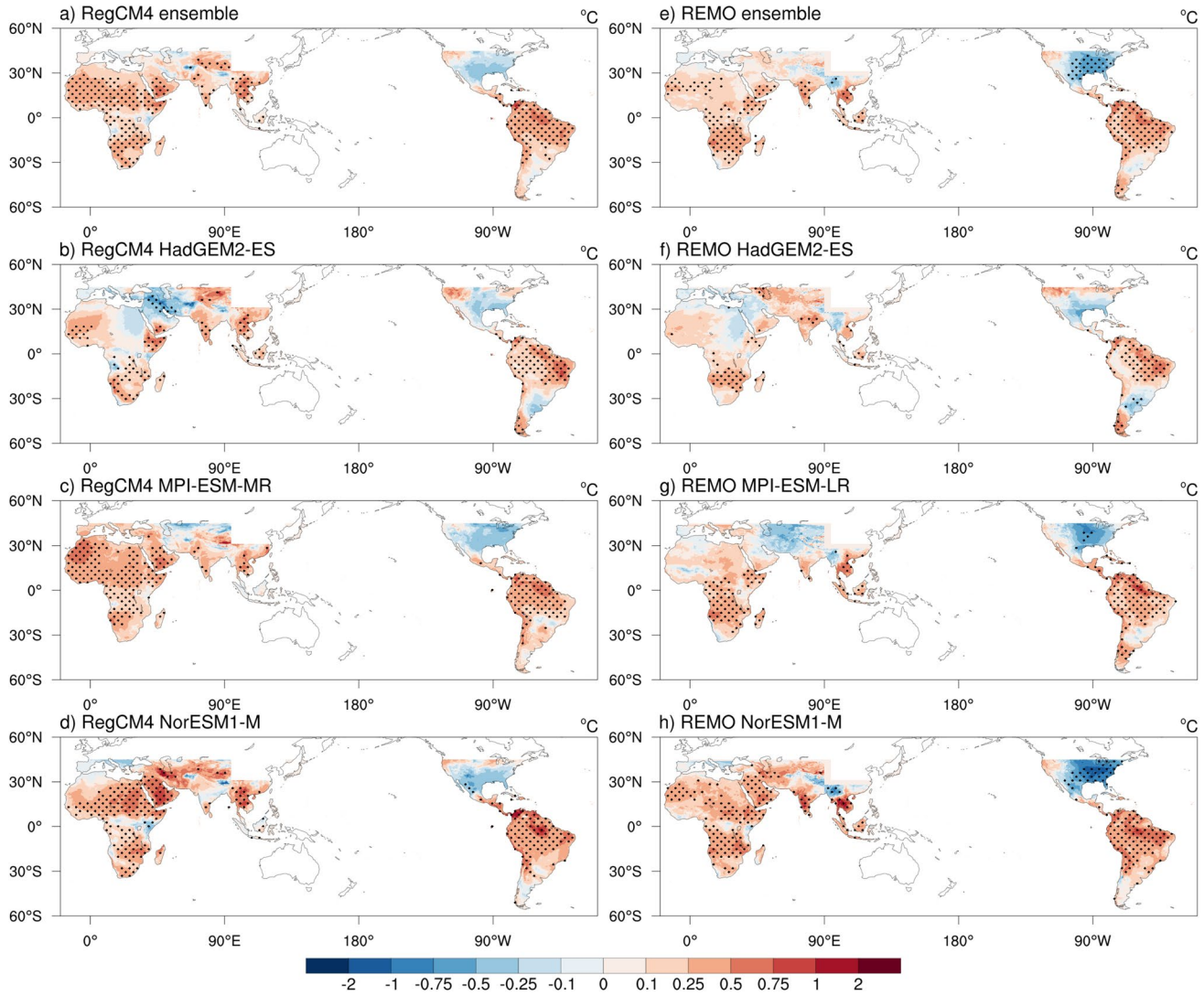

Fig. 11 As in Fig. 7, but for 2-m air surface temperature. The units are °C

Overall, according to our results for ensembles and individual simulations, the RCM with higher resolution does not always produce more accurate ENSO temperature teleconnection patterns compared to the driving GCMs. We also note that, although REMO tends to produce lower temperature biases than RegCM4 (see Sect. 3.1), it does not produce consistently better teleconnection responses.

4 Concluding remarks

We analyzed the ENSO teleconnection patterns for boreal cold season (DJF) precipitation and surface air temperature in an ensemble of CORDEX-CORE historical simulations with two RCMs driven by 3 GCMs. The focus of the analysis is on five regions where the ENSO signal is strong. In general, we find that the RCMs preserve the broad scale teleconnection signals of the driving GCMs despite the use of large, continental scale domains. Therefore, the interannual variability of the GCMs is not substantially modified by the RCM nesting. Another general conclusion is that the ensemble averages and the individual simulations show teleconnection signals statistically significant at the 95% significance level, over most of the regions analysed.

For temperature both the GCM and RCM ensembles, as well as most individual simulations exhibit a good performance in reproducing the ENSO signal over different regions of the World, with some statistically significant responses. However, we do not find a clear added value in the use of RCMs because the signal itself has a broad regional scale structure. For precipitation, the models also show a good performance in reproducing most of the observed regional scale teleconnection signals. In these cases, the signals are characterized by finer scale structure, which is better

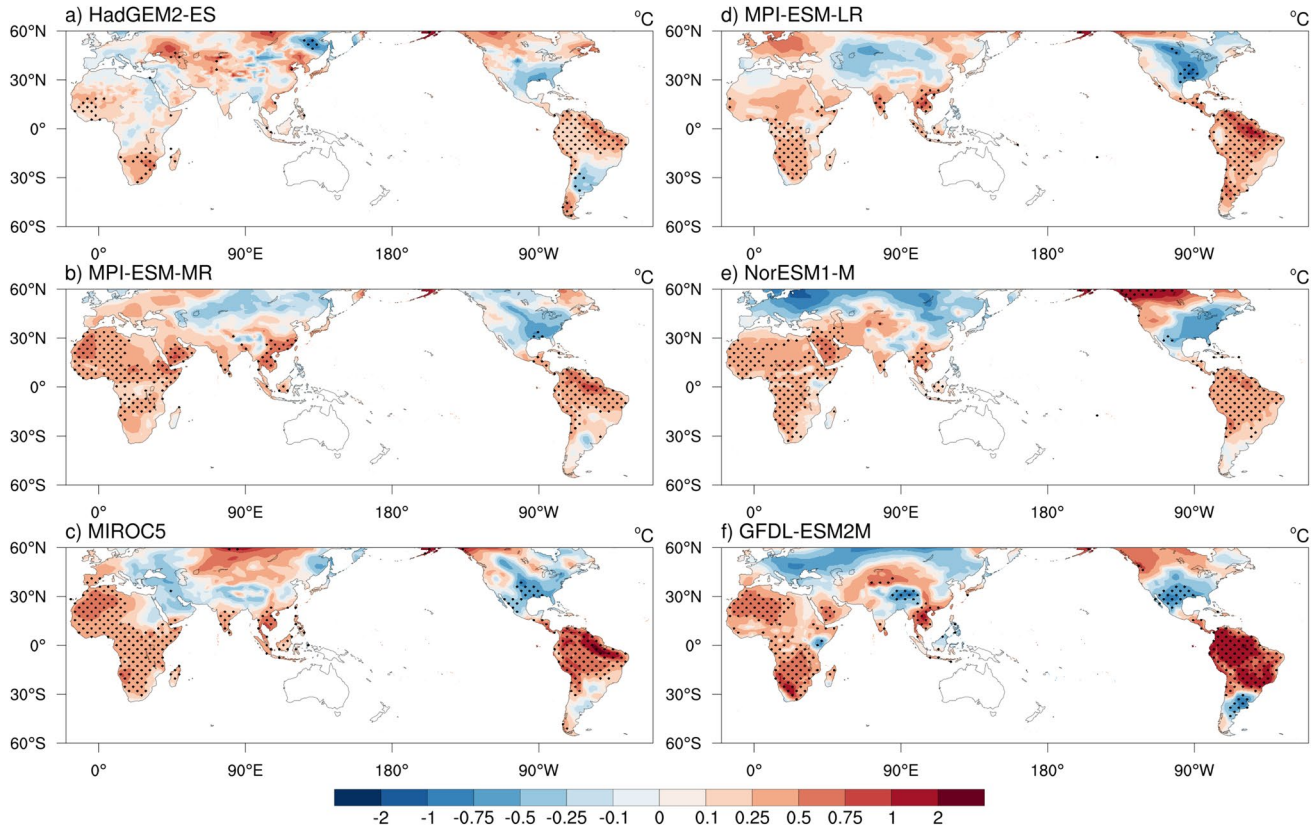

Fig. 12 As in Fig. 8, but for 2-m air surface temperature. The units are °C

captured over most regions by the RCMs, in particular concerning the magnitude of the spatial variability of the signal. Comparing the performance of the RegCM4 and REMO, we found that the RegCM4 ensemble produced a more realistic ENSO signal in precipitation and temperature over Africa and the region composed of Mexico and the southern United States, while REMO has a better signal over Southeast Asia, particularly for temperature. In addition, the RegCM4 simulations mostly exhibit a more accurate amplitude in teleconnection patterns.

In general, it is difficult to identify the origins of specific differences between GCMs and RCMs and across the two different RCM ensembles, because these may depend on a multiplicity of causes, such as resolution, use of different physics schemes and local morphological features. This is particularly the case in view of the fact that there are not systematic differences across models, but these depend on the variables and regions considered. Therefore, such identification requires in-depth targeted analyses which are beyond the scope of the present paper. For the same reason, an eventual user of the data is encouraged to use the output from all models available in order to assess related uncertainties.

Despite this consideration, our study clearly shows that GCM-RCM downscaling systems produce a realistic signal of ENSO teleconnections over different regions, and thus are valuable tools not only in a climate change research context, but also in seasonal to annual prediction. In particular, the latter is an area that should be better explored in terms of RCM application (e.g. Giorgi 2019), especially given that it is now possible to run RCMs at convection permitting resolutions (1–3 km) (Coppola et al. 2018), thereby having the

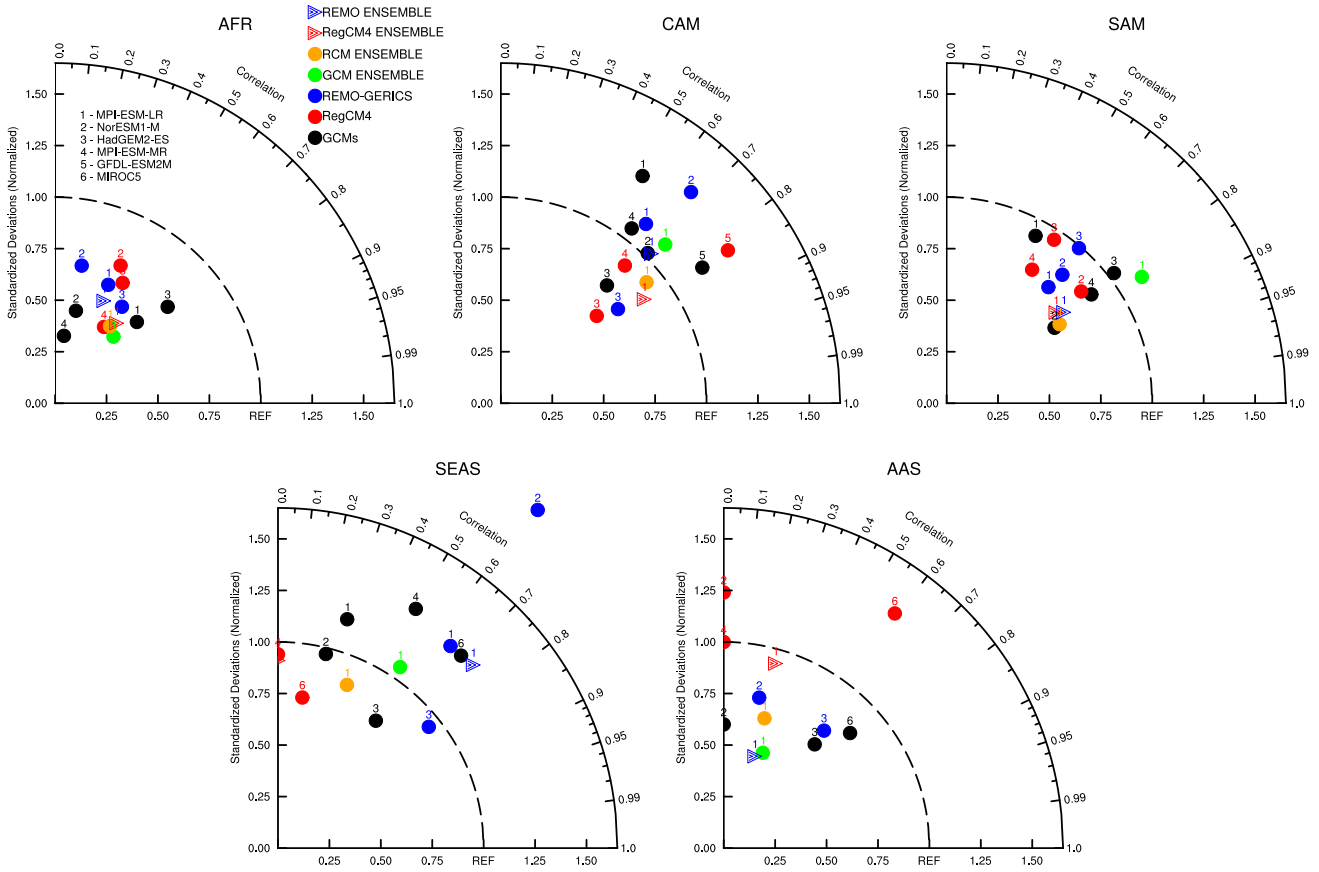

Fig. 13 As in Fig. 9, but for 2-m air surface temperature

potential to provide information down to the local scales. We plan to extend the present analysis to the twenty-first century future segment of the CORDEX-CORE experiments to assess simulated changes in ENSO teleconnection patterns.

Acknowledgements We greatly appreciate the comments and suggestions of the editor and two anonymous reviewers, which helped improve this manuscript. The RegCM4 simulations for the ICTP institute have been completed thanks to the support of the CINECA supercomputing center, Bologna, Italy and the ISCRA projects HP10BDU7TR and HP10BQCFJ2. The authors would like to thank Graziano Giuliani and Ivan Girotto for their constant support in the preparation of the simulations used in this paper. The authors would also like to thank the CMIP5, as well as the ESGF for providing access to their database where most of the data is available. The study was also supported by the Oak Ridge Leadership Computing Facility and the National Climate-Computing Research Center at the Oak Ridge National Laboratory and the Climate Service Center Germany (GERICS), Helmholtz-Zentrum Geesthacht, Hamburg, Germany; all of whom provided access to their simulation data. The observations were provided by the Met Office (https://www.metoffice.gov.uk/hadobs/hadisst/), Hylke Beck, the developer of the MSWEP data (http://www.gloh2o.org/) and the Climate Data Store (CDS) of the European Centre for Medium Range Weather Forecasts (ECMWF-ERA5; https://cds.climate.copernicus.eu/cdsapp#!/dataset/reanalysis-era5-single-levels-monthly-means?tab=form)

References

Abid MA, Almazroui M, Kucharski F et al (2018) ENSO relationship to summer rainfall variability and its potential predictability over Arabian Peninsula region. NPJ Clim Atmos Sci 1:1. https://doi.org/10.1038/s41612-017-0003-7

Achuta Rao K, Sperber K (2006) ENSO simulations in coupled ocean-atmosphere models: are the current models better? Clim Dyn 27:1–16

Ashfaq M et al (2017) Sources of errors in the simulation of south Asian summer monsoon in the CMIP5 GCMs. Clim Dyn 49(1–2):193–223

Beck HE, van Dijk AIJM, Levizzani V, Schellekens J, Miralles DG, Martens B, de Roo A (2017a) MSWEP: 3-hourly 0.25° global gridded precipitation (1979–2015) by merging gauge, satellite, and reanalysis data. Hydrol Earth Syst Sci 21:589–615

Beck HE et al (2017b) Global-scale evaluation of 22 precipitation datasets using gauge observations and hydrological modeling. Hydrol Earth Syst Sci 21:6201–6217

Bellenger H, Guilyardi E, Leloup J, Lengaigne M, Vialard J (2013) ENSO representation in climate models: from CMIP3 to CMIP5. Clim Dyn 42:1999–2018

Bentsen M, Bethke I, Debernard JB, Iversen T, Kirkevåg A, Seland Ø, Drange H, Roelandt C, Seierstad IA, Hoose C, Kristjansson JE (2013) The norwegian earth system model, NORESM1-M - part 1: description and basic evaluation of the physical climate. Geosci Model Dev 6(3):687–720

Boulard D, Pohl B, Crétat J, Vigaud N (2012) Downscaling large-scale climate variability using a regional climate model: the case of ENSO over Southern Africa. Clim Dyn 40:1141–1168

Bretherton CS, Park S (2009) A new moist turbulence parameterization in the community atmosphere model. J Clim 22:3422–3448

Bretherton CS, McCaa JR, Grenier H (2004) A new parameterization for shallow cumulus convection and its application to marine subtropical cloud-topped boundary layers. I. Description and 1D results. Mon Weather Rev 132:864–882

Cai W, van Rensch P, Cowan T, Sullivan A (2010) Asymmetry in ENSO teleconnection with regional rainfall, its multidecadal variability, and impact. J Clim 23:4944–4955

Cash BA, Schneider EK, Bengtsson L (2005) Origin of regional climate differences: role of boundary conditions and model formulation in two GCMs. Clim Dyn 25:709–723. https://doi.org/10.1007/s00382-005-0069-5

Chiodi AM, Harrison DE (2015) Equatorial Pacific easterly wind surges and the onset of La Niña events. J Clim 28:776–792. https://doi.org/10.1175/JCLI-D-14-00227.1

Coelho CAS, Goddard L (2009) El Nino-induced tropical droughts in climate change projections. J Clim 22:6456–6476

Coppola E, Sobolowski S, Pichelli E et al (2018) A first-of-its-kind multi-model convection permitting ensemble for investigating convective phenomena over Europe and the Mediterranean. Clim Dyn. https://doi.org/10.1007/s00382-018-4521-8

Coppola E, Raffaele F, Giorgi F et al (2020) Climate hazard indices projections based on CORDEX-CORE, CMIP5, CMIP6 ensembles. Clim Dyn (submitted)

da Rocha RP, Reboita MS, Dutra LMM, Llopart M, Coppola E (2014) Interannual variability associated with ENSO: present and future climate projections of RegCM4 for South America-CORDEX domain. Clim Change 125:95–109

Diaz HF, Hoerling MP, Eischeid JK (2001) ENSO variability, teleconnections and climate change. Int J Climatol 21:1845–1862

Dieppois B, Rouault M, New M (2015) The impact of ENSO on southern African rainfall in CMIP5 ocean atmosphere coupled climate models. Clim Dyn 45:2425–2442

Dunne JP et al (2012) GFDL's ESM2 global coupled climate-carbon earth system models. Part I: physical formulation and baseline simulation characteristics. J Clim 25:6646–6665

Elguindi N, Giorgi F, Turuncoglu UU (2014) Assessment of CMIP5 global model simulations over the sub-set of CORDEX domains used in the phase I CREMA experiment. Clim Change. https://doi.org/10.1007/S10584-013-0935-9

Emanuel K (1991) A scheme for representing cumulus convection in large scale models. J Atmos Sci 48:2313–2335

Endris HS, Omondi P, Jain S et al (2013) Assessment of the performance of CORDEX regional climate models in simulating east Africa Rainfall. J Clim 26:8453–8475

Endris HS, Lennard C, Hewitson B et al (2018) Future changes in rainfall associated with ENSO, IOD and changes in the mean state over Eastern Africa. Clim Dyn 52:2029–2053

Giorgetta MA, Jungclaus JH et al (2013) Climate and carbon cycle changes from 1850 to 2100 in MPI-ESM simulations for the coupled model intercomparison project phase 5. J Adv Model Earth Syst 5(3):572–597

Giorgi F (2019) Thirty years of regional climate modeling: where are we and where are we going next? J Geophys Res Atmos 124:5696–5723

Giorgi F, Gutowski WJ (2015) Regional dynamical downscaling and the CORDEX initiative. Annu Rev Environ Resour 40:467–490

Giorgi F, Coppola E, Solmon F, Mariotti L et al (2012) RegCM4: model description and preliminary tests over multiple CORDEX domains. Clim Res 52:7–29

Grenier H, Bretherton CS (2001) A moist PBL parameterization for large-scale models and its application to subtropical cloud-topped marine boundary layers. Mon Weather Rev 129:357–377

Guilyardi E et al (2004) Representing El Niño in coupled ocean–atmosphere GCMs: the dominant role of the atmospheric component. J Clim 17:4623–4629

Guilyardi E, Braconnot P, Jin F-F, Kim ST, Kolasinski M, Li T, Musat I (2009) Atmosphere feedbacks during ENSO in a coupled GCM with a modified atmospheric convection scheme. J Clim 22:5698–5718

Gutowski WJ Jr, Giorgi F, Timbal B, Frigon A, Jacob D, Kang HS, Raghavan K, Lee B, Lennard C, Nikulin G, O'Rourke E, Rixen M, Solman S, Stephenson T, Tangang F (2016) WCRP coordinated regional downscaling experiment (CORDEX): a diagnostic MIP for CMIP6. Geosci Model Dev 9:4087–4095. https://doi.org/10.5194/gmd-9-4087-2016

Herceg Bulić I (2010) The sensitivity of climate response to the wintertime Niño3.4 sea surface temperature anomalies of 1855–2002. Int J Climatol. https://doi.org/10.1002/joc.2255

Herceg Bulić I, Kucharski F (2012) Delayed ENSO impact on spring precipitation over North/Atlantic European region. Clim Dyn 38:2593–2612. https://doi.org/10.1007/s00382-011-1151-9

Hersbach H, Dee D (2016) ERA5 reanalysis is in production, ECMWF Newsletter, vol 147, p 7. https://www.ecmwf.int/en/newsletter/147/news/era5-reanalysis-production. Accessed 14 Nov 2019

Holtslag A, de Bruijn E, Pan H-L (1990) A high resolution air mass transformation model for short range weather forecasting. Mon Weather Rev 118:1561–1575

Jacob D, Elizalde A, Haensler A, Hagemann S, Kumar P, Podzun R, Rechid D, Remedio AR, Saeed F, Sieck K, Teichmann C, Wilhelm C (2012) Assessing the transferability of the regional climate model REMO to different coordinated regional climate downscaling experiment (CORDEX) regions. Atmosphere 3(1):181–199. https://doi.org/10.3390/atmos3010181

Jiang P, Gautam MR, Zhu J, Yu Z (2013) How well do the GCMs/RCMs capture the multi-scale temporal variability of precipitation in the Southwestern United States? J Hydrol 479:75–85. https://doi.org/10.1016/j.jhydrol.2012.11.041

Jones CD, Hughes JK, Bellouin N, Hardiman SC, Jones GS, Knight J, Liddicoat S, O'Connor FM, Andres RJ, Bell C, Boo KO, Bozzo A, Butchart N, Cadule P, Corbin KD, Doutriaux-Boucher M, Friedlingstein P, Gornall J, Gray L, Halloran PR, Hurtt G, Ingram WJ, Lamarque JF, Law RM, Meinshausen M, Osprey S, Palin EJ, Parsons Chini L, Raddatz T, Sanderson MG, Sellar AA, Schurer A, Valdes P, Wood N, Woodward S, Yoshioka M, Zerroukat M (2011) The HadGEM2-ES implementation of CMIP5 centennial simulations. Geosci Model Dev 4(3):543–570. https://doi.org/10.5194/gmd-4-543-2011

Joseph R, Nigam S (2006) ENSO evolution and teleconnections in IPCC's twentieth-century climate simulations: realistic representation? J Clim 19:4360–4377

Kain J-S (2004) The Kain-Fritsch convective parameterization: an update. J Appl Meteorol 43(1):170–181

Kain J-S, Fritsch J-M (1990) A one-dimensional entraining/detraining plume model and its application in convective parameterization. J Atmos Sci 47(23):2784–2802

Kayano MT, Pestrelo de Oliveira C, Andreoli RV (2009) Interannual relations between South American rainfall and tropical sea surface temperature anomalies before and after 1976. Int J Climatol 29:1439–1448

King AD, Vincent CL (2018) Using global and regional model simulations to understand Maritime Continent wet-season rainfall variability. Geophys Res Lett 45(12):534–543

King AD, van Oldenborgh GJ, Karoly DJ (2016) Climate change and El Niño increase likelihood of Indonesian heat and drought. Bull Am Meteorol Soc 97(12):113–117

Kucharski F, Bracco A, Yoo JH, Molteni F (2007) Low-frequency variability of the Indian monsoon-ENSO relationship and the tropical Atlantic: the "weakening" of the 1980s and 1990s. J Clim. https://doi.org/10.1175/jcli4254.1

Langenbrunner B, Neelin JD (2013) Analyzing ENSO teleconnections in CMIP models as a measure of model fidelity in simulating precipitation. J Clim 26:4431–4446

Latif M, Sperber K, Arblaster J, Braconnot P, Chen D, Colman A, Cubasch U, Cooper C et al (2001) ENSIP: the El Niño simulation intercomparison project. Clim Dyn 18:255–276

Llopart M, Coppola E, Giorgi F, da Rocha R, Cuadra SV (2014) Climate change impact on precipitation for the Amazon and La Plata basins. Clim Change 125(1):111–125

Lohmann U, Roeckner E (1996) Design and performance of a new cloud microphysics scheme developed for the ECHAM4 general circulation model. Clim Dyn 12:557–572

Louis JF (1979) A parametric model of vertical eddy fluxes in the atmosphere. Bound Layer Meteorol 17(2):187–202

Manly BF (1997) Randomization and Monte Carlo methods in biology, 2nd edn. Chapman & Hall, New York

Mariotti L, Coppola E, Sylla MB, Giorgi F, Piani C (2011) Regional climate model simulation of projected 21st century climate change over an all-Africa domain: comparison analysis of nested and driving model results. J Geophys Res. https://doi.org/10.1029/2010JD015068

McGlone D, Vuille M (2012) The associations between El Niño-Southern Oscillation and tropical South American climate in a regional climate model. J Geophys Res 117:D06105. https://doi.org/10.1029/2011JD017066

McPhaden MJ, Zebiak SE, Glantz MH (2006) ENSO as an integrating concept in earth science. Science 314:1739–1745

McSweeney CF, Jones RG, Lee RW et al (2015) Selecting CMIP5 GCMs for downscaling over multiple regions. Clim Dyn 44:3237. https://doi.org/10.1007/s00382-014-2418-8

Meque A, Abiodun B (2015) Simulating the link between ENSO and summer drought in southern Africa using regional climate models. Clim Dyn 44:1881–1900

Nordeng TE (1994) Extended versions of the convective parametrization scheme at ECMWF and their impact on the mean and transient activity of the model in the tropics. Tech. rep., ECMWF Research Department, European Centre for Medium Range Weather Forecasts, Reading, UK

Pal J-S, Small E-E, Eltahir E-A-B (2000) Simulation of regional scale water and energy budgets: representation of subgrid cloud and precipitation processes within RegCM. J Geophys Res 105(D24):29579–29594

Pfeifer S (2006) Modeling cold cloud processes with the regional climate model REMO. PhD thesis, University of Hamburg

Philander SG (1990) El Niño, La Niña, and the southern oscillation. International geophysics series, vol 46. Academic Press, San Diego

Ratna SB, Ratnam JV, Behera SK, Tangang FT, Yamagata T (2017) Validation of the WRF regional climate model over the subregions of Southeast Asia: climatology and interannual variability. Clim Res 71:263–280. https://doi.org/10.3354/cr01445

Rayner NA et al (2003) Global analyses of sea surface temperature, sea ice, and night marine air temperature since the late nineteenth century. J Geophys Res 108:4407

Remedio AR, Teichmann C, Buntemeyer L, Sieck K, Weber T, Rechid D, Hoffmann P, Nam C, Kotova L, Jacob D (2019) Evaluation of new CORDEX simulations using an updated Köppen-Trewartha climate classification. Atmosphere 10(11):726

Ropelewski CF, Halpert MS (1987) Global and regional scale precipitation patterns associated with the El Niño/Southern Oscillation. Mon Weather Rev 115:1606–1626

Spencer H, Slingo JM (2003) The simulation of peak and delayed ENSO teleconnections. J Clim 16(11):1757–1774

Stevens B, Giorgetta M, Esch M et al (2013) Atmospheric component of the MPI-M earth system model: ECHAM6. J Adv Model Earth Syst 5:146–172. https://doi.org/10.1002/jame.20015

Taylor AB, MacKinnon DP (2012) Four applications of permutation methods to testing a single-mediator model. Behav Res 44:806–844. https://doi.org/10.3758/s13428-011-0181-x

Taylor KE, Stouffer RJ, Meehl GA (2012) An overview of CMIP5 and the experiment design. Bull Am Meteorol Soc 78:485–498

Teichmann C, Jacob D, Remedio AR, Remke T, Buntemeyer L, Hoffmann P et al (2020) Assessing mean climate change signals in the global CORDEX-CORE ensemble. Clim Dyn (submitted)

Tiedtke M (1989) A Comprehensive mass flux scheme for cumulus parameterization in large-scale models. Mon Weather Rev 117(8):1779–1800

Tiedtke M (1996) An extension of cloud-radiation parameterization in the ECMWF model: the representation of subgrid-scale variations of optical depth. Mon Weather Rev 124:745–750. https://doi.org/10.1175/1520-0493(1996)124%3C0745:AEOCRP%3E2.0.CO;2

Torres-Alavez et al (2020) Future projections in tropical cyclone activity over multiple CORDEX domains from RegCM4 CORDEX-CORE simulations. Clim Dyn (submitted)

Tourigny E, Jones C (2009) An analysis of regional climate model performance over the tropical Americas. Part ii: simulating subseasonal variability of precipitation associated with ENSO forcing. Tellus 61A:343–356

Trenberth KE, Kumar A, Karoly D, Ropelewski C, Branstator GW, Lau N-C (1998) Progress during TOGA in understanding and modeling global teleconnections associated with tropical sea surface temperatures. J Geophys Res Ocean 103:14291–14324

Wallace JM, Gutzler DS (1981) Teleconnections in the geopotential height field during the northern hemisphere winter. Mon Weather Rev 109:784

Wang B, Kang I-S, Lee J-Y (2004) Ensemble simulations of Asian-Australian monsoon variability by 11 AGCMS. J Clim 17:803–818

Ward PJ, Jongman B, Kummu M, Dettinger MD, Weiland FCS, Winsemius HC (2014) Strong influence of El Niño Southern Oscillation on flood risk around the world. Proc Natl Acad Sci USA 111:15659–15664. https://doi.org/10.1073/pnas.1409822111

Watanabe M et al (2010) Improved climate simulation by MIROC5: mean states, variability, and climate sensitivity. J Clim 23:6312–6335

Weare BC (2013) El Niño teleconnections in CMIP5 models. Clim Dyn 41:2165–2177

Whan K, Zwiers F (2016) The impact of ENSO and NAL on extreme winter precipitation in North America in observations and regional climate models. Clim Dyn 48:1401–1411

Zaroug MAH, Giorgi F, Coppola E, Abdo GM, Eltahir EAB (2014) Simulating the connections of ENSO and the rainfall regime of East Africa and the upper Blue Nile region using a climate model of the tropics. Hydrol Earth Syst Sci 18:4311–4323. https://doi.org/10.5194/hess-18-4311-2014

Zeng X, Zhao M, Dickinson R-E (1998) Intercomparison of bulk aerodynamic algorithms for the computation of sea surface fluxes using TOGA COARE and TAO data. J Clim 11(10):2628–2644

Zhang W, Villarini G, Vecchi GA, Murakami H (2019) Rainfall from tropical cyclones: high-resolution simulations and seasonal forecasts. Clim Dyn. https://doi.org/10.1007/s00382-018-4446-2